Research Square

Preprints are preliminary reports that have not undergone peer review.
They should not be considered conclusive, used to inform clinical practice,
or referenced by the media as validated information.

Geochemistry of the Paleocene saline lake in the southwestern Jianghan Basin, Central China: implications for provenance, tectonic setting, and palaeoclimate

Kai Yan
Chinese Academy of Geological Sciences
Chunlian Wang (wangchunlian321@163.com)
Chinese Academy of Geological Sciences
Jiuyi Wang
Chinese Academy of Geological Sciences
Xiaocan Yu
Chinese Academy of Geological Sciences
Xiaohua Teng
Zaozhuang University
Ruiqin Li
Peking University
Lihong Liu
China Geological Survey

Research Article

Keywords: The Jianghan Basin, Geochemistry, Provenance, Tectonic setting, Palaeoclimate

Posted Date: April 22nd, 2022

DOI: https://doi.org/10.21203/rs.3.rs-1525762/v1

License: This work is licensed under a Creative Commons Attribution 4.0 International License.
Read Full License

Abstract

As an important sedimentary area of mineral resources in central and eastern China, the Jianghan Basin has received more and more attention. In recent years, thick evaporites and potassium and lithium-rich brine ores have been discovered in the Paleocene strata in the southern Jianghan Basin, which provides a material basis for studying the genesis of evaporites in central and eastern China. This paper aims to further understand the provenance, tectonic setting and paleoenvironment of the Paleocene Shashi Formation in the south of Jianghan Basin through the study of whole-rock geochemistry, so as to provide theoretical basis for the formation of evaporite. The chondrite-normalized REE distribution pattern of the Shashi Formation's siltstones are characterized by enriched LREE and flat HREE similar to those of UCC with negative Eu anomalies. Combined with the geochemical element ratio discriminant diagram, such as Al_2O_3-TiO_2, Zr/Sc-Th/Sc, Hf-La/Th, and La/Sc-Co/Th, these samples were sourced from felsic source rocks. Moreover, the discriminant diagrams of K_2O/Na_2O-SiO_2/Al_2O_3, La-Th-Sc, and Th-Co-Zr/10 suggest that the samples were formed under the tectonic settings of active continental margin and continental island arc. The discriminant diagrams of Zr/Sc-Th/Sc and Al_2O_3-Zr-TiO_2 show that all samples were not affected by recycling and hydraulic sorting. The weathering indices (CIA, CIW, PIA, and ICV) and the diagram of Al_2O_3-(CaO + Na_2O)-K_2O suggest that mild chemical weathering in the source area under arid climatic condition. And the palaeoclimatic indicators of Sr/Cu, Ga/Rb, and C-value indicate that the climate was cool and arid. According to the geochemical data and previous studies, the Paleocene sediments in the southwest of the Jianghan Basin were from felsic source rocks, and formed in the tectonic background of active continental margin and continental island arc, and the climate was mainly arid and cold.

Introduction

The Jianghan Basin is a Mesozoic-Cenozoic rift basin in central China, which has experienced multi-stage tectonic movement. In the Paleocene, the Jianghan Basin deposited abundant evaporites and potassium and lithium-rich brine ore (Wang et al. 2013, 2020; Liu 2013; Shen et al. 2014; Liu et al. 2015). Due to the complex tectonic movement, extremely arid paleoclimate type and various material sources in the Jianghan Basin, it is difficult for us to study the genesis of evaporite minerals. In view of the sedimentary characteristics of evaporite in a series of rifted basins in south China, Liu et al. (2013, 2016) proposed that the formation of evaporite deposits was controlled by tectonics, provenance and climate. Based on this view, a lot of studies on the origin of evaporites and deep brine have been carried out in recent years (Wang et al. 2016, 2021; Shen et al. 2014; Yu et al. 2018a, 2018b; Yan et al. 2018; Yu et al. 2020). And based on the analysis of geochemical data from the Paleocene Shashi Formation mudstone from Well ZK0303 in the southwestern Jianghan Basin, this paper reveals the provenance, tectonic setting and sedimentary environment of the clastic sediments in the saline lake.

After many years of development, geochemical parameters have been widely used in paleoenvironmental conditions, tectonic setting and clastic rock provenance (Nesbitt and Young 1982; Bhatia 1983;

McLennan et al. 1995). And the composition of clastic sedimentary rocks is controlled by a combination of factors such as parent rock composition, weathering (physical and chemical), transport, sedimentation, and diagenesis. The formation of avaporite depends on the coupling of provenance, tectonic setting and climate, among which climate plays a decisive role (Liu 2013). Previous studies showed that the southwest of the Jianghan Basin had diverse provenance (Yu et al. 2018a), frequent tectonic activity (Wang 2006; Wang et al. 2018) and arid and hot climate (Sun and Wang 2005) during Paleocene. The geochemical characteristics of the sediments can reveal all these factors and provide reliable basis for the deposition of evaporite. And the latest geochemical data also provide new insights, such as that the climate was not hot at all.

Study area

The Jianghan Basin located in the Yangtze Block of central China, is a large Mesozoic-Cenozoic rift basin, with a total area of 36,360 km^2 (Gilder et sl. 1991; Teng et al. 2019). It is bordered by the Qinling orogen in the north, the Dabie Terrance in the northeast, the Edong fold-thrust belt in the east, the Jiangnan orogen in the south, and the Huangling massif and the Xiang'exi fold-thrust belt in the west (Fig. 1A; Hu et al. 2006a; Shen et al. 2012; Wu et al. 2017). The Presinian metamorphic basement of the Jianghan Basin was formed during the Late Proterozoic. The basement of the Jianghan Basin consists of two parts: the underlying crystalline basement and the overlying pre-rift strata. The crystalline basement of the Jianghan Basin mainly consists of Archean-Proterozoic metamorphic and metasedimentary rocks (HBGMR 1990). During the Ediacaran to the early Triassic, with the influence of the regional Indosinian movement spreading to this area, the Jianghan Basin uplifted to different degrees under the background of dramatic and rapid crustal rise, and the sea water slowly withdrew westward, forming a set of extensive coastal clastic rocks interbedded with marine carbonate rocks (Dai 1996; Yao et al. 2015). The middle Triassic to Jurassic sediments in the Jianghan Basin were mainly terrestrial conglomerate, sandstone and mudstone, and interbedded with coal seams formed from Carboniferous to early Triassic Period (HBGMR 1990; Shu et al. 2008). Under the influence of the Yanshanian movement, a NW-trending fault belt was formed in the Jianghan Basin from late Jurassic to early Cretaceous (Wang et al. 2006; Hu et al. 2006b). From the late Cretaceous to Paleogene, the Jianghan Basin experienced the active upwelling of the upper mantle induced by the rolling of the Pacific plate and the Indo-Asian collision, resulting in multi-stage rifting and the formation of extensive siliceous clasts, evaporites and a large number of basalts in the basin, and finally formed the present geographical characteristics (Liu et al. 2004; Li et al. 2015).

The Jianghan Basin is composed of several secondary structural units and depressions. The Jiangling depression is the largest secondary negative tectonic unit in Jianghan Basin, which was formed on the Yanshanian fold basement under the depression setting of late Cretaceous to Paleogene (Fig. 1B). The growth and development of Jiangling depression are controlled by Qingshuikou fault, Jishansi fault, Wen'ansi fault and Gong'an-Songzi fault, and divided into two independent units by Wancheng fault (Fig. 2; Yang et al. 2003; Wang et al. 2013; Yu et al. 2018b). In 2016, we obtained a 2,302.03 m long well

(ZK0303) in the southwest of the Jiangling depression. The core is mainly composed of purplish pink siltstone and dark gray mudstone, interbedded with anhydrite, glauberite and halite.

Materials And Methods

A total of 35 siltstone samples were collected from Well ZK0303 based on the criteria of vertical differences (Fig. 2). We split the core ZK0303 into two halves in the longitudinal, and selected the fresh part that was not contaminated. All samples were stored in plastic bags to avoid secondary pollution and oxidation as much as possible. Under microscope, the clastic composition of these samples are composed of quartz, feldspar, and lithic. Among them, the lithic grains are subangular to subrounded, and lithic fragments are mainly sedimentary rock, with less volcanic and metamorphic rocks. Sedimentary lithic grains are mainly composed of chert (Fig. 3b, d, e, and f), mudstone and siltstone (Fig. 3a, c, e, and f), while the metamorphic grains are mainly quartzite (Fig. 3a, c, d). No significant volcanic debris are found in the samples. Feldspar grains are subangular, mainly plagioclase (Fig. 3a, b, f). Quartz grains are subrounded to angular, mainly monocrystalline quartz, visible polycrystalline quartz (Fig. 3). Most monocrystalline quartz is clear without inclusions. The individual crystals of the polycrystalline quartz grains have straight to slightly curved intercrystal boundaries. The matrixes and cements are dominated by mudstone, calcite, and anhydrite (Fig. 3).

Before the geochemical analysis all samples were air-dried, crushed to 200 mesh and thoroughly mixed. The major elements were analyzed by X-ray fluorescence spectrometer (XRF), and the trace and rare earth elements were tested by inductively coupled plasma mass spectrometry (ICP-MS). After that, the powdered samples were heated and poured into the mixture of anhydrous lithium tetraborate, lithium fluoride and ammonium nitrate to melt into glass sheets, which were continued to be heated in a muffle furnace to determine loss on ignition. Finally, the fused samples were heated to 800°C and analyzed using a sequential X-ray fluorescence spectrometer (AB104L, Axios-mAX). Calibrations of accuracy and reproducibility were conducted using the GB/T 14506.14–2010 and GB/T 14506.28–2010 standards. Precision for major elements are within 1%.

The content of trace and rare earth elements were measured by inductively coupled plasma mass spectrometer (ICP-MS, ELEMENT XR). Heat the powdered samples with HF and HNO_3. After evaporation to dryness, HNO_3 was added to dissolve the samples. Then, HNO_3 was added to samples again and heated to 130°C. Finally, the distilled water was added to the solution and the contents of trace elements were measured. Calibrations of accuracy and reproducibility were conducted using the GB/T 14506.30–2010 and HDB/T 3022 – 2018. Precision for trace and rare earth elements are within 5%. All geochemical analyses were carried out in the Analytical Laboratory Beijing Research Institute of Uranium Geology.

Results

Among the major elements, the average contents of SiO_2 (48.27%), Al_2O_3 (14.01%) and CaO (8.00%) are the top three (Supplementary Table S1). And almost contents of SiO_2, Al_2O_3, TiO_2 and MnO show relative

depletion after they are normalized to the Average Post-Archean Australian Shale (PAAS) (Fig. 4A). In contrast, the contents of all CaO and MgO were higher than those of PAAS and show strong enrichment (Fig. 4A).

The three elements with the highest average content are Sr, Ba and Rb, and their average contents are 2307.74 ppm, 393.60 ppm and 154.60 ppm, respectively (Supplementary Table S1). The preservation state of each element varies greatly if they are normalized to Average Upper Continental Crust (UCC) data. The contents of Cr and Cs are enriched relative to UC, the contents of Nb, Ta, Zr and Hf show strong depletion (Fig. 4B).

For REE, the Ce contents range from 47 to 88 ppm, averaging 64.07 ppm, the La contents range from 25.60 to 46.90 ppm, averaging 36.18 ppm, and the Nd contents range from 22.10 to 40.00 ppm, averaging 30.35 ppm (Supplementary Table S1). They are the three most abundant REEs. The LREE/HREE ratios range from 7.91 to 11.86, averaging 8.96 (Table 1). The Eu/Eu* ratios generally show negative anomalies, and they range from 0.62 to 0.83 (average = 0.70) (Table 1). In the chondrite-normalized diagram (Fig. 4C), the light REE (LREE) ratios show strong enrichment, while heavy REE (HREE) ratios show flat enrichment.

Table 1
Ratios of selected elements of the Paleocene siltstones in the Jianghan Basin

No.	LREE/HREE	Eu/Eu*	CIA	CIW	PIA	ICV	C-value	Sr/Cu	Ga/Rb
ZK1	9.06	0.68	55.33	63.50	57.17	1.63	0.31	40.00	0.13
ZK2	8.70	0.71	45.77	51.23	44.62	1.88	0.25	10.02	0.14
ZK3	8.36	0.76	48.03	53.51	47.53	1.83	0.25	14.63	0.15
ZK4	8.68	0.77	47.02	53.10	46.14	1.72	0.28	15.07	0.13
ZK5	8.04	0.79	59.06	69.46	62.93	1.30	0.46	15.04	0.14
ZK6	8.29	0.83	40.54	44.89	38.27	2.18	0.25	15.62	0.12
ZK7	8.33	0.68	56.03	65.34	58.44	1.67	0.31	83.85	0.12
ZK8	8.35	0.71	60.54	72.32	65.63	1.44	0.41	11.04	0.12
ZK9	11.86	0.66	59.99	70.51	64.23	1.32	0.40	10.35	0.12
ZK10	8.47	0.66	47.92	54.53	47.25	1.94	0.26	34.78	0.10
ZK11	13.83	0.62	61.51	73.11	66.86	1.44	0.38	23.13	0.09
ZK12	9.35	0.74	45.41	50.52	44.24	2.03	0.21	665.00	0.11
ZK13	8.48	0.64	62.38	74.40	68.29	1.32	0.46	10.30	0.11
ZK14	8.90	0.66	59.04	69.75	63.04	1.44	0.37	31.48	0.10
ZK15	9.58	0.72	65.46	78.08	72.84	1.27	0.44	36.14	0.11
ZK16	9.00	0.72	63.87	76.32	70.59	1.27	0.43	18.59	0.11
ZK17	8.58	0.77	48.06	54.35	47.47	1.78	0.27	14.17	0.12
ZK18	8.60	0.71	52.70	60.98	53.71	1.63	0.35	14.56	0.11
ZK19	8.37	0.69	53.24	60.86	54.32	1.70	0.25	79.48	0.11
ZK20	8.62	0.67	61.63	71.94	66.30	1.43	0.32	212.27	0.11
ZK21	8.71	0.73	54.25	62.35	55.74	1.58	0.35	134.67	0.12
ZK22	8.54	0.69	48.62	55.21	48.19	1.76	0.27	123.43	0.11
ZK23	10.23	0.68	36.79	40.23	34.05	2.39	0.15	840.48	0.11
ZK24	8.37	0.74	64.44	76.26	70.92	1.36	0.39	27.34	0.11
ZK25	8.88	0.66	46.88	52.21	46.08	1.86	0.28	15.53	0.13
ZK26	8.48	0.73	50.45	57.35	50.59	1.77	0.30	81.42	0.11
ZK27	9.21	0.62	38.44	42.49	35.72	2.34	0.18	59.03	0.10

No.	LREE/HREE	Eu/Eu*	CIA	CIW	PIA	ICV	C-value	Sr/Cu	Ga/Rb
ZK28	9.08	0.68	63.48	76.60	70.50	1.29	0.48	6.24	0.10
ZK29	8.98	0.66	58.35	68.58	61.90	1.35	0.36	38.67	0.09
ZK30	7.91	0.71	62.91	74.55	68.77	1.27	0.47	6.45	0.11
ZK31	7.97	0.68	55.78	64.18	57.83	1.45	0.34	9.53	0.12
ZK32	8.27	0.70	39.49	43.15	37.35	2.46	0.18	526.04	0.11
ZK33	8.33	0.77	43.93	49.31	42.24	2.03	0.27	7.07	0.10
ZK34	10.42	0.67	55.47	64.53	57.61	1.50	0.32	98.96	0.10
ZK35	8.83	0.70	52.63	60.44	53.55	1.63	0.31	9.23	0.10

Discussion

Provenance

The geochemical data are often used to identify the provenance and reveal the characteristics of the source area (Roser and Korsch 1986; Cullers 1995; Armstrong-Altrin et al. 2013). As essential immobile elements, the ratios of of Al, Ti, and Zr can be used to reflect the type of the original rock (Stumm and Morgan 1981; Wesolowski 1992; Ayers and Watson 1993; Hayashi et al. 1997). In the plots of TiO_2 versus Al_2O_3, Hayashi et al. (1997) divided the provenance into three types: mafic igneous rocks, intermediate igneous rocks, and felsic igneous rocks. And the samples of the Shashi Formation mainly belong to the source area of intermediate and felsic igneous rocks (Fig. 5A). Apart from the major elements, some trace elements (La, Sc, Cr, Hf, Th, Zr, etc.) and REEs are of great significance in interpreting the provenance and composition of the source area because of their potential nature of low mobility during the post-depositional process (Bhatia and Crook 1986; Mclennan et al. 1993). On the diagram of Th/Sc versus Zr/Sc (McLennan et al. 1993), all samples were also concentrated near the felsic source rocks, and the trend for Zr enrichment indicates that the sediment compositions of all samples may be not affected by recycling (Fig. 5B). On the diagram of La/Th versus Hf (Floyd and Leveridge 1987), all of the samples fall around the felsic arc source region (Fig. 5C). And on the Co/Th versus La/Sc diagram proposed by McLennan et al. (1993), these samples are located between andesite and felsic source rocks (Fig. 5D). In addition, the REE distribution and Eu anomaly in the sediments can also provide clues for the research of the source characteristics (Cullers 1994). The high LREE/HREE ratios and negative Eu anomalies of the Shashi Formation show the characteristics of felsic source rocks (Table 1; Fig. 4C). And the siltstone samples are mainly quartz, followed by feldspar, without basic clasts, indicating felsic source rocks. In general, these samples have the characteristics of felsic source rocks.

Tectonic setting

Previous studies have showen that the bulk-rock geochemistry of siliciclastic sediments is affected by the tectonic movement of source rocks, so it is often used to distinguish the tectonic setting of sedimentary basins (Bhatia 1983; Roser and Korsch 1986; Bhatia and Crook 1986). Some trace elements (such as La, Th, Sc, and Zr) with relatively low mobility can not only be used to trace the source rock but also be an important basis to distinguish tectonic setting. The tectonic setting of sediment development can be roughly divided into four types (Taylor and McLennan 1985; Bhatia and Crook 1986): oceanic island arc (OA), continental island arc (CA), active continental margin (ACM), and passive margin (PM). On the diagram of Th-Co-Zr/10 (Fig. 6A), most samples of the Shashi Formation fall around the ACM field; on the diagram of La-Th-Sc (Fig. 6B), most of samples are located at the CA (Bhatia and Crook 1986). And on the diagram of SiO_2/Al_2O_3 versus K_2O/Na_2O (Roser and Korsch 1986) (Fig. 6C), almost all samples are located at ACM field.

Jianghan Basin is a rift basin in a composite basin-mountain system, and its sediments are provided by the erosion of elevated tectonic units that include various basement sequences. Yu et al. (2018a) identified four provenances with different orientations based on the U-Pb ages of zircons and bulk geochemical characteristics of clastic rocks of the Paleocene Shashi Formation. The oldest zircons are from Paleoproterozoic-Archean, and the geochemical data indicate that these samples are from the passive continental margin, characterized by recycled sedimentary, and are believed to have originated from the Huangling uplift in the northwest Jianghan Basin (Yu et al. 2018a). The second set of zircon ages are Neoproterozoic. During which magmatism associated with the Rodinian Supercontinent rupture was widespread in South China (Li et al. 2003a, 2003b; Zheng et al. 2004; Greentree et al. 2006), and Neoproterozoic volcanic rocks were also prevalent in the basement of the surrounding range systems of the Jianghan Basin, such as the South Qinling Belt, the Jiangnan Orogen, and Huangling uplift (Wang et al. 2007; Liu et al. 2008; Yao et al. 2013; Li and Zhao 2016). So, these samples of zircon are probably from basement of the ranges around the Jianghan Basin. The last set of zircons are from Ordovician-Triassic. The Ordovician zircons were derived from Caledonian magmatism in the Jiangnan Orogen (Shu et al. 1991; Ren 1991; Wang et al. 2011) and the North Dabashan zone of the South Qinling Belt (Chen et al. 2014; Cao et al. 2015; Wang et al. 2015), while the Triassic zircons were major derived from Indosinian magmatism in the Jiangnan Orogen (Yue et al. 1998; Wang et al. 2002, 2005). And the synthesis of geochemical data and petrographic results indicates felsic source rocks in the active continental margin and continental arc (Yu et al. 2018a). These indicate that the Jianghan Basin received detrital materials from the South Qinling Belt in the north and the Jiangnan Orogen in the south.

The siltstone samples of the Paleocene Shashi Formation in well ZK0303 also have the characteristics of felsic source rocks in the active continental margin and continental arc. According to the analysis of Yu et al. (2018), the provenance of the Paleocene in well ZK0303 should be mainly from the South Qinling Belt in the north and the Jiangnan Orogen in the south.

Palaeoweathering and palaeoclimate

In arid climate, the source rocks are mainly affected by physical weathering, in which they can only be mechanically broken down into smaller grain sizes without significant changes in mineralogical and chemical composition (Wanas and Assal 2020). And the chemical weathering plays a dominant role in humid climates and strongly controls the major and trace element composition of siliceous clastic sediments (Nesbitt and Young 1982; Harnois 1988; Middelburg et al.1988; McLennan et al. 1993; Fedo et al. 1995). It directly affects the removal of mobile elements (Na, K, Ca) and the enrichment of immobile elements (Al, Si) in the sediments (Nesbitt and Young 1982). The chemical index of alteration (CIA = $Al_2O_3/(Al_2O_3 + CaO^* + Na_2O + K_2O) \times 100$, Nesbitt and Young 1982; $CaO^* = CaO - 10/3 \times P_2O_5$, McLennan et al. 1993) and Al_2O_3-($CaO + Na_2O$)-K_2O (A-CN-K) ternary diagram (Nesbitt and Young 1984) can determine the mobility of elements during chemical weathering and potassium metasomatism during diagenesis, and evaluate the weathering history and source rock composition. Besides, chemical index of weathering (CIW = $Al_2O_3/(Al_2O_3 + CaO + Na_2O) \times 100$, Harnois 1988), plagioclase index of alteration (PIA = $100\times (Al_2O_3 - K_2O)/(Al_2O_3 + CaO^* + Na_2O - K_2O)$, Fedo et al. 1995), and index of compositional variability (ICV= $(Fe_2O_3 + K_2O + Na_2O + CaO + MgO + TiO_2)/Al_2O_3$, Cullers et al. 1995) are also important bases for assessing the source area palaeoweathering.

The ratios of CIA in the all samples vary from 36.79 to 65.46 (average = 53.30) (Table 1). In general, a CIA ratio of 55 or less represents unweathered, while 100 represents fully weathered (Nesbitt and Young 1982). The lower CIA ratio indicates that chemical weathering in the source area was less during the Paleocene. In the ternary diagram of A-CN-K (Fig. 7A), All the samples are near the boundary of A-CN and are distributed along the line between clinopyroxene and PAAS, away from the A-K boundary that represents high weathering. And the ratios of CIW range from 40.23 to 78.08 (average = 61.60), the ratios of PIA range from 34.05 to 72.84 (average = 55.17), the ratios of ICV range from 1.27 to 2.39 (average = 1.66) (Table 1), They all represent a low to moderate degree of weathering in the source area (Harnois 1988; Fedo et al. 1995). In addition, the ternary diagram of Al_2O_3-Zr-TiO_2 indicates that hydraulic sorting is not obvious (Fig. 7B, Garcia et al. 1991).

Worash (2002) believes that the distribution, composition and relative concentration of some trace elements in clastic rocks may indicate the palaeoclimate and palaeoenvironment. Zhao et al. (2007) and Cao et al. (2012) proposed using C-value as an indicator of palaeoclimate. The calculation formula of C-value is as follows: C-value = Σ(Fe + Mn + Cr + V + Ni + Co)/Σ(Ca + Mg + Sr + Ba + K + Na). This is because the Fe, Mn, Cr, V, Ni and Co elements are relatively enrich in humid conditions, while in arid conditions, evaporation precipitates saline minerals, resulting in the concentration of Ca, Mg, K, Na, Sr and Ba elements. And some current studies have shown that palaeoclimate conditions can impact the ratios of Ga/Rb, Rb/Sr and Sr/Cu in sediments (Jin and Zhang 2002; Bai et al. 2015). Gallium is related to kaolinite, suggesting strong chemical weathering associated with warm and humid climatic conditions (Roy and Roser 2013). Rubidium is enriched in illite, reflecting a dry and cold climate associated with weak chemical weathering (Beckmann et al. 2005). In the warm sedimentary environment, the ratio of Rb/Sr in sediments decreases, while the ratio of Sr/Cu increases (Lerman and Gat 1989; Cao et al. 2015).

And the Sr/Cu ratio between 1.3 and 5.0 represents humid environments, while the Sr/Cu ratio is higher than 5.0 in arid climates (Lerman 1978).

On the major elements diagram (Suttner and Dutta 1986), all samples are located at arid field (Fig. 8A). And the C-value range from 0.15 to 0.48, Sr/Cu ratios range from 6.24 to 840.48, and Ga/Rb ratios range from 0.09 to 0.15 (Table 1). According to the C-value and Sr/Cu ratio (Zhao et al. 2007 and Cao et al. 2012), the climatic conditions of the Paleocene Shashi Formation were between arid and semi-arid/semi-humid (Fig. 8B). Moreover, the projection points in the Sr/Cu- Ga/Rb discriminant map indicate that the Jianghan Basin had a cold and arid climate during the Paleocene (Fig. 8C). Comprehensive geochemical indicators, climate of the Jianghan Basin was cold and arid during the Paleocene.

Conclusions

(1) The REE distribution and Al_2O_3-TiO_2, La/Sc-Co/Th, Hf-La/Th and Zr/Sc-Th/Sc ratios of the clastic rocks in Shashi Formation indicate that the southwestern Jianghan basin mainly received felsic source rocks during the Paleocene.

(2) Based on the analysis of the data of major and trace elements, the Paleocene clastic rocks in Jianghan Basin were formed under the tectonic background of active continental margin and continental island arc with frequent faulting activities.

(3) And the ratios of CIA, CIW, PIA, and ICV indicates low weathering in the source area. The ratios of Sr/Cu, Ga/Rb, and C-values reflect the cool and arid climate of the Paleocene in the Jianghan Basin.

Declarations

Data Availability

Data is available based on request.

Conflicts of Interest

The authors declare that they have no conflicts of interest.

Author Contributions Statement

K.Y. and C.L.W. wrote the main manuscript text. J.Y.W., X.C.Y. and X.H.T. developed the idea for the study. R.Q.L. and L.H.L. analyzed the data. All authors reviewed the manuscript.

Acknowledgments

We appreciate the funding by grants from the Central Public Welfare Scientific Research Basic Scientific Research Business Expenses (No. KK2005), the National Natural Science Foundation of China (Nos.

U20A2092, 42002106, 41907262 and 41502089), the Major State Basic Research Development Program of China (No. 2011CB403007) and the China Geological Survey (No. DD20190606).

References

1. Armstrong-Altrin JS, Nagarajan R, Madhavaraju J, Rosalez-Hoz L, Lee YI, Balaram V, Cruz-Martinez A, Avila-Ramirez G (2013) Geochemistry of the Jurassic and upper Cretaceous shales from the Molango Region, Hidalgo, Eastern Mexico: implications of source-area weathering, provenance, and tectonic setting. C R Geosci 345: 185–202.
2. Ayers JC, Watson EB (1993) Rutile solubility and mobility in supercritical aqueous fluids. Contrib Mineral Petrol 114: 321–330.
3. Bai Y, Liu Z, Sun P, Liu R, Hu X, Zhao H, Xu Y (2015) Rare earth and major element geochemistry of Eocene fine-grained sediments in oil shale- and coal-bearing layers of the Meihe Basin, northeast China. J Asian Earth Sci 97: 89–101.
4. Beckmann B, Flögel S, Hofmann P, Schulz M, Wagner T (2005) Orbital forcing of Cretaceous river discharge in tropical Africa and ocean response. Nature 437(7056): 241–244.
5. Bhatia MR (1983) Plate tectonics and geochemical composition of sandstones. J Geol 93: 611–627.
6. Bhatia MR, Crook KA (1986) Trace element characteristics of graywackes and tectonic setting discrimination of sedimentary basins. Contrib Mineral Petrol 92: 181–193.
7. Boynton WV (1984) Geochemistry of the rare earth elements: Meteorite studies. In: Henderson P. (ed) Rare Earth Element Geochemistry. Elsevier, Amsterdam, pp63–114.
8. Cao HS, Guo W, Shan XL, Ma L, Sun PC (2015) Paleolimnological environments and organic accumulation of the Nenjiang Formation in the southeastern Songliao Basin. Oil Shale 32: 5–24.
9. Cao J, Wu M, Chan Y, Hu K, Bian LZ, Wang LG, Zhang Y (2012) Trace and rare earth elements geochemistry of Jurassic mudstones in the northern Qaidam basin, northwest China. Geochemistry 72: 245–252.
10. Cao L, Zhang Q, Hu SJ, Duan QF, Zhou Y, Yu YS, Zou XW, Gan JM (2015) LA-ICP-MS zircon U-Pb age of diabase porphyry from the Donghe area, Fangxian in South Daba Mountain and its tectonic significance. Acta Geologica Sinia 89: 2314–2322.
11. Chen H, Tian M, Wu GL, Hu JM (2014) The Early Paleozoic alkaline and mafic magmatic events in Southern Qinling Belt, Central China: evidences for the break-up of the Paleo-Tethyan Ocean. Geol Rev 60:1437–1452.
12. Chen WT, Zhou M, Zhao X (2013) Late Paleoproterozoic sedimentary and mafic rocks in the Hekou area, SW China: Implication for the reconstruction of the Yangtze Block in Columbia. Precambrian Res 231: 61–77.
13. Cullers RL (1994) The controls on the major and trace element variation of shales, siltstones, and sandstones of Pennsylvanian-Permian age from uplifted continental blocks in Colorado to platform in Kansas, USA. Geochim Cosmochim Acta 58: 4955–4972.

14. Cullers RL (1995) The controls on the major- and trace-element evolution of shales, siltstones and sandstones of Ordovician to Tertiary age in the wet mountains region, Colorado, USA. Chem Geol 123: 107–131.
15. Dai SW (1996) Discussion on the regional structural features of Jianghan Basin since the indosinian movement. J Geomech 04: 82–86.
16. Fedo CM, Nesbitt HW, Young GM (1995) Unraveling the effects of potassium metasomatism in sedimentary rocks and paleosoils, with implications for paleoweathering conditions and provenance. Geology 23: 921–924.
17. Floyd PA, Leveridge BE (1987) Tectonic environment of the Devonian Gramscatho Basin, South Cornwall: framework mode and geochemical evidence from turbiditic sandstones. J Geol Soc (London, U.K.) 144: 531–542.
18. Garcia D, Coelho J, Perrin M (1991) Fractionation between TiO_2 and Zr as a measure of sorting within shale and sandstone series (northern Portugal). Eur J Mineral 3: 401–414.
19. Gilder SA, Keller GR, Luo M, Goodell PC (1991) Eastern asia and the western pacific timing and spatial distribution of rifting in china. Tectonophysics 197: 225–243.
20. Greentree MR, Li ZX, Li XH, Wu HC (2006) Late Mesoproterozoic to earliest Neoproterozoic basin record of the Sibao orogenesis in western South China and relationship to the assembly of Rodinia. Precambrian Res 151: 79–100.
21. Harnois L (1988) The CIW index: a new chemical index of weathering. Sediment. Geol. 55: 319–322.
22. Hayashi KI, Fujisawa H, Holland HD, Ohmoto H (1997) Geochemistry of ~ 1.9 Ga sedimentary rocks from northeastern Labrador, Canada. Geochim Cosmochim Acta 61: 4115–4137.
23. HBGMR (Hubei Bureau of Geology and Mineral Resources) (1990) Regional Geology of the Hubei Province. Geological Press, Beijing.
24. Hu SB, Kohn BP, Raza A, Wang J, Gleadow AJW (2006a) Cretaceous and Cenozoic cooling history across the ultrahigh pressure Tongbai–Dabie belt, central China, from apatite fission-track thermochronology. Tectonophysics 420: 409–429.
25. Hu SB, Raza A, Min K, Kohn BP, Reiners PW, Ketcham RA, Wang YY, Gleadlow AJW (2006b) Late Mesozoic and Cenozoic thermotectonic evolution along a transect from the north China craton through the Qinling orogen into the Yangtze craton, central China. Tectonics 25: TC6009.
26. Jin ZD, Zhang EL (2002) Paleoclimate implications of Rb/Sr ratios from lake sediments. Sci Technol Eng 2: 20–22.
27. Lerman A (1978) Lakes: Chemistry, Geology, Physics. Springer-Verlag, New York.
28. Lerman ADI, Gat J (1989) Physics and Chemistry of Lakes. Springer-Verlag, Berlin.
29. Li QW, Zhao JH (2016) Petrogenesis of the Wudang mafic dikes: implication of changing tectonic settings in South China during the Neoproterozoic. Precambrian Res 272: 101–114.
30. Li XH, Li ZX, Ge W, Zhou H, Li W, Liu Y, Wingate MTD (2003a) Neoproterozoic granitoids in South China: crustal melting above a mantle plume at 825 Ma? Precambrian Res 122: 45–83.

31. Li XY, Zhu PM, Kusky TM, Gu Y, Peng SB, Yuan YF, Fu JM (2015) Has the Yangtze craton lost its root? A comparison between the North China and Yangtze cratons. Tectonophysics 655: 1–14.
32. Li ZX, Li XH, Kinny PD, Wang J, Zhang S, Zhou H (2003b) Geochronology of Neoproterozoic syn-rift magmatism in the Yangtze Craton, South China and correlations with other continents: evidence for a mantle superplume that broke up Rodinia. Precambrian Res 122: 85–109.
33. Liu CL (2013) Characteristics and formation of potash deposits in continental rift basins: a review. Acta Geosci Sin 34: 515–527.
34. Liu CL, Yu XC, Zhao YJ, Wang JY, Wang LC, Xu HM, Li J, Wang CL (2016) A tentative discussion on regional metallogenic background and mineralization mechanism of subterranean brines rich in potassium and lithium in south China block. Miner Deposits (Beijing, China) 35: 1119–1143.
35. Liu CL, Zhao YJ, Fang XM, Lv FL, Wang LC, Yan MD, Zhang H, Ding, T (2015) Plate tectonic control on the distribution and formation of the marine potash deposits. Acta Geol Sin 89: 1893–1907.
36. Liu M, Cui XJ, Liu FT (2004) Cenozoic rifting and volcanism in eastern China: a mantle dynamic link to the Indo-Asian collision? Tectonophysics 393: 29–42.
37. Liu XM, Gao S, Diwu CR, Ling WL (2008) Precambrian crustal growth of Yangtze Craton as revealed by detrital zircon studies. Am J Sci 308: 421–468.
38. McLennan SM (1989) Rare earth elements in sedimentary rocks: influence of provenance and sedimentary processes. Rev Mineral Geochem 21: 169–200.
39. McLennan SM, Hemming S, McDaniel DK, Hanson GN (1993) Geochemical approaches to sedimentation, provenance, and tectonics. In: Johanson MJ, Basu A (eds) Processes controlling the composition of clastic sediments. Geological Society of America, special paper 284, USA, pp 21–40.
40. McLennan SM, Hemming SR, Taylor SR, Eriksson KA (1995) Early Proterozoic crustal evolution: geochemical and Nd-Pb isotopic evidence from metasedimentary rocks, southwestern North America. Geochim Cosmochim Acta 59: 1153–1177.
41. Middelburg JJ, Van der Weijden CH, Woittiez JRW (1988) Chemical processes affecting the mobility of major, minor and trace elements during weathering of granitic rocks. Chem Geol 68: 253–273.
42. Nesbitt HW, Young GM (1982) Early Proterozoic climates and plate motions inferred from major element chemistry of lutites. Nature 299: 715–717.
43. Nesbitt HW, Young GM (1984) Prediction of some weathering trends of plutonic and volcanic-rocks based on thermodynamic and kinetic considerations. Geochim Cosmochim Acta 48: 1523–1534.
44. Ren JS (1991) On the geotectonics of southern China. Acta Geological Sinica (English Edition) 64: 111–136.
45. Roser BP, Korsch RJ (1986) Determination of tectonic setting of Sandstones-mudstone suites using SiO_2 content and K_2O/Na_2O ratio. The J Geol 94: 635–650.
46. Roy DK, Roser BP (2013) Climatic control on the composition of Carboniferous-Permian Gondwana sediments, Khalaspir basin, Bangladesh. Gondwana Res 23: 1163–1171.

47. Sarki Yandoka BM, Abdullah WH, Abubakar MB, Hakimi MH, Adegoke AK (2015) Geochemical characterisation of Early Cretaceous lacustrine sediments of Bima Formation, Yola sub-basin, Northern Benue trough, NE Nigeria: Organic matter input, preservation, paleoenvironment and palaeoclimatic conditions. Mar Pet Geol 61: 82–94.
48. Shen C, Donelick RA, O'Sullivan PB, Jonckheere R, Yang Z, She Z, Miu X, Ge X (2012) Provenance and hinterland exhumation from LA-ICP-MS zircon U-Pb and fission-track double dating of Cretaceous sediments in the Jianghan Basin, Yangtze block, central China. Sediment Geol 281: 194–207.
49. Shen LJ, Liu CL, Xu HM, Wang CL, Wang LC, Liu BK, Zhang LB (2014) Paleocene mineral assemblage characteristics of Jianghan depression and their significance for potash formation. Miner Deposits (Beijing, China) 33: 1020–1030.
50. Shu LS, Charvet J, Shi YS, Faure M, Cluzel D, Guo LZ (1991) Structural analysis of the Nanchang-Wanzai sinistral ductile shear zone (Jiangnan region, South China). J Asian Earth Sci 6: 13–23.
51. Shu LS, Faure M, Wang B, Zhou XM, Song B (2008) Late Palaeozoic-Early Mesozoic geological features of South China: Response to the Indosinian collision events in Southeast Asia. C R Geosci 340: 151–165.
52. Stumm W, Morgan JJ (1981) Aquatic Chemistry, Wiley, New York.
53. Sun XJ, Wang PX (2005) How old is the Asian monsoon system?-Palaeobotanical records from China. Palaeogeogr Palaeoclimatol Palaeoecol 222: 181–222.
54. Suttner LJ, Dutta PK (1986) Alluvial sandstone composition and paleoclimate I. Framework mineralogy. J Sediment Res 56: 329–345.
55. Taylor SR, McLennan SM (1985) The Continental Crust: Its Composition and Evolution. Blackwell Scientific Publications, Oxford, UK.
56. Teng XH, Fang XM, Alan JK, Liu CL, Wang JY, Zan JB, Yang YB, Wang CL, Xu HM, Ruth FS, Nadine MP (2019) Sedimentological and mineralogical records from drill core SKD1 in the Jianghan Basin, Central China, and their implications for late Cretaceous-early Eocene climate change. J Asian Earth Sci 182: 103936.1-103936.14.
57. Wanas HA, Assal EM (2020) Provenance, tectonic setting and source area-paleoweathering of sandstones of the Bahariya Formation in the Bahariya Oasis, Egypt: An implication to paleoclimate and paleogeography of the southern Neo-Tethys region during Early Cenomanian. Sediment Geol 413: 105822.
58. Wang BJ (2006) Episodic tectonic movement and evolutional character in Jianghan Basin. Oil Geophysical Prospecting 41: 226–230.
59. Wang CL, Liu CL, Wang JY, Yu XC, Yan K (2020) Palynology and stratigraphy of the thick evaporate-bearing Shashi Formation in Jiangling Depression, Jianghan Basin of South China, and its paleoclimate change. China Geol 3: 283–291.
60. Wang CL, Liu CL, Xu HM, Wang LC, Zhang LB (2013) Carbon and oxygen isotopes characteristics of Paleocene saline lake facies carbonates in Jiangling depression and their environmental significance. Acta Geosci Sinica 34: 567–576.

61. Wang CL, Liu CL, Yu XC, Li HN, Liu JL (2016) The extremely hot and dry climatic events and potash enrichment in salt lakes. Acta Geol Sin (Engl Ed) 90: 769–770.
62. Wang CL, Yu XC, Li RQ, Liu LH, Liu CL, Yan K, You C (2021) Origin of lithium-potassium-rich brines in the Jianghan Basin, south China: constraints by water-rock reactions of Mesozoic-Cenozoic igneous rocks. Minerals 11: 1330.
63. Wang DL, Mei LF, Liu YS, Wu LL, Min CZ, Luo J (2018) Mesozoic-Cenozoic episodic subsidence and Migration of Jianghan Basin in extensional composite Basin-Mountain system. J China Univ Geosci 43: 4180–4192.
64. Wang KM, Wang ZQ, Zhang YL, Wang G (2015a) Geochronology and Geochemistry of Mafic Rocks in the Xuhe, Shaanxi, China: Implications for Petrogenesis and Mantle Dynamics. Acta Geol Sin 89: 187–202.
65. Wang XL, Zhou JC, Griffin WL, Wang RC, Qiu JS, O'Reilly SY, Xu XS, Liu XM, Zhang GL (2007) Detrital zircon geochronology of Precambrian basement sequences in the Jiangnan Orogen: dating the assembly of the Yangtze and Cathaysia blocks. Precambrian Res 159:117–131.
66. Wang YJ, Zhang AM, Fan WM, Zhao GC, Zhang GW, Zhang YZ, Zhang FF, Li SZ (2011) Kwangsian crustal anatexis within the eastern South China Block: geochemical, zircon U-Pb geochronological and Hf isotopic fingerprints from the gneissoid granites of Wugong and Wuyi-Yunkai domains. Lithos 127: 239–260.
67. Wang YJ, Zhang YH, Fan WM, Peng TP (2005) Structural signatures and $^{40}Ar/^{39}Ar$ geochronology of the Indosinian Xuefengshan tectonic belt, South China. J Struct Geol 27: 985–998.
68. Wang YJ, Zhang YH, Fan WM, Xi XW, Guo F, Lin G (2002) Numerical modeling for generation of Indo-Sinian peraluminous granitoids Hunan Province: basaltic underplating vs. tectonic thickening. Sci China (Series D) 45: 1042–1056.
69. Wesolowski DJ (1992) Aluminum speciation and equilibria in aqueous solution: I. The solubility of gibbsite in the system Na-K-Cl-OH-Al (OH)4 from 0 to 100°C. Geochim Cosmochim Acta 56: 1065–1091.
70. Worash G (2002) Geochemistry provenance and tectonic setting of the Adigrat sandstone northern Ethiopia. J Afr Earth Sci 35: 185–198.
71. Wu LL, Mei LF, Liu YS, Luo J, Min CZ, Lu SL, Li MH, Guo LB (2017) Multiple provenance of rift sediments in the composite basin-mountain system: constraints from detrital Zircon U-Pb geochronology and heavy minerals of the early Eocene Jianghan Basin, Central China. Sediment Geol 349: 46–61.
72. Yan K, Liu CL, Wang JY, Wang CL, Xu HM, Wang CL, Yu XC, Meng LY (2018) Sulfur isotopic characteristics of Eocene series in the Yanjing- Shenjindu sub-depression in the southern Jiangling depression and its implication for paleoclimate and provenance. Acta Geol Sin 92: 1647–1660.
73. Yang CQ, Chen KQ, Cheng ZQ, Zhan HJ (2003) Constituent evolution and exploration potential in Jianghan depression. Nat Gas Ind 23: 51–54.

74. Yao JL, Shu LS, Santosh M, Li JY (2013) Geochronology and Hf isotope of detrital zircons from Precambrian sequences in the eastern Jiangnan Orogen: Constraining the assembly of Yang-tze and Cathaysia Blocks in South China. J Asian Earth Sci 74: 225–243.
75. Yao WH, Li ZX, Li WX, Su L, Yang JH (2015) Detrital provenance evolution of the Ediacaran-Silurian Nanhua foreland basin, South China. Gondwana Res 28: 1449–1465.
76. Yu XC, Liu CL, Wang CL, Li F, Wang JY (2020) Eolian deposits of the northern margin of the south China (Jianghan Basin): reconstruction of the Late Cretaceous East Asian landscape in central China. Mar Pet Geol 117: 104390.
77. Yu XC, Liu CL, Wang CL, Wang JY, Xu HM, Li HN (2018b) Sedimentary characteristics and palaeoclimatic significance of glauberite in Paleocene lacustrine deposits of the Jiangling depression, central China. Geosci J 22: 1–16.
78. Yu XC, Liu CL, Wang CL, Xu HM (2018a) Provenance of rift sediments in a composite basin-mountain system: constraints from petrography, whole-rock geochemistry, and detrital zircon U-Pb geochronology of the Paleocene Shashi Formation, southwestern Jianghan Basin, central China. Int J Earth Sci 107: 1–26.
79. Yue HY, Shu LS, Wang JF, Zhang J (1998) A study on geothermal history and uplifting mechanism for the Wugongshan granite in Wugongshan mountain, south China in the Mesozoic. Geotectonica et Metallogenia 22: 227–233.
80. Zhao ZY, Zhao JH, Wang HJ, Liao JD, Liu CM (2007) Distribution characteristics and applications of trace elements in Junggar Basin. Na Gas Explor Dev 30: 30–33.
81. Zheng YF, Wu YB, Chen FK, Gong B, Li L, Zhao ZF (2004) Zircon U-Pb and oxygen isotope evidence for a large-scale ^{18}O depletion event in igneous rocks during the Neoproterozoic. Geochim Cosmochim Acta 68: 4145–4165.

Figures

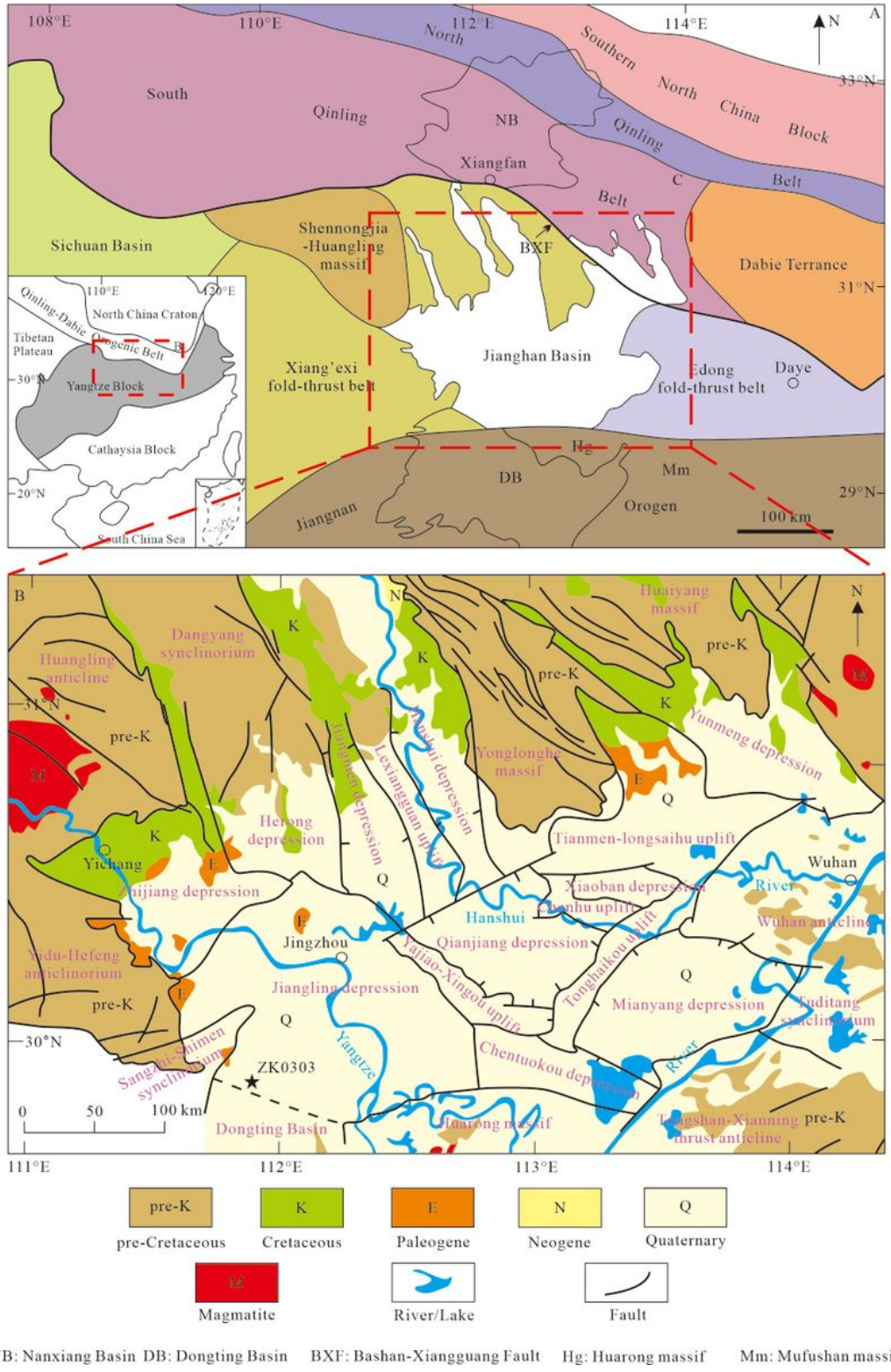

NB: Nanxiang Basin DB: Dongting Basin BXF: Bashan-Xiangguang Fault Hg: Huarong massif Mm: Mufushan massif

Figure 1

Geologic and tectonic sketch maps of the Jianghan Basin region. (A) modified after Chen et al. (2013).

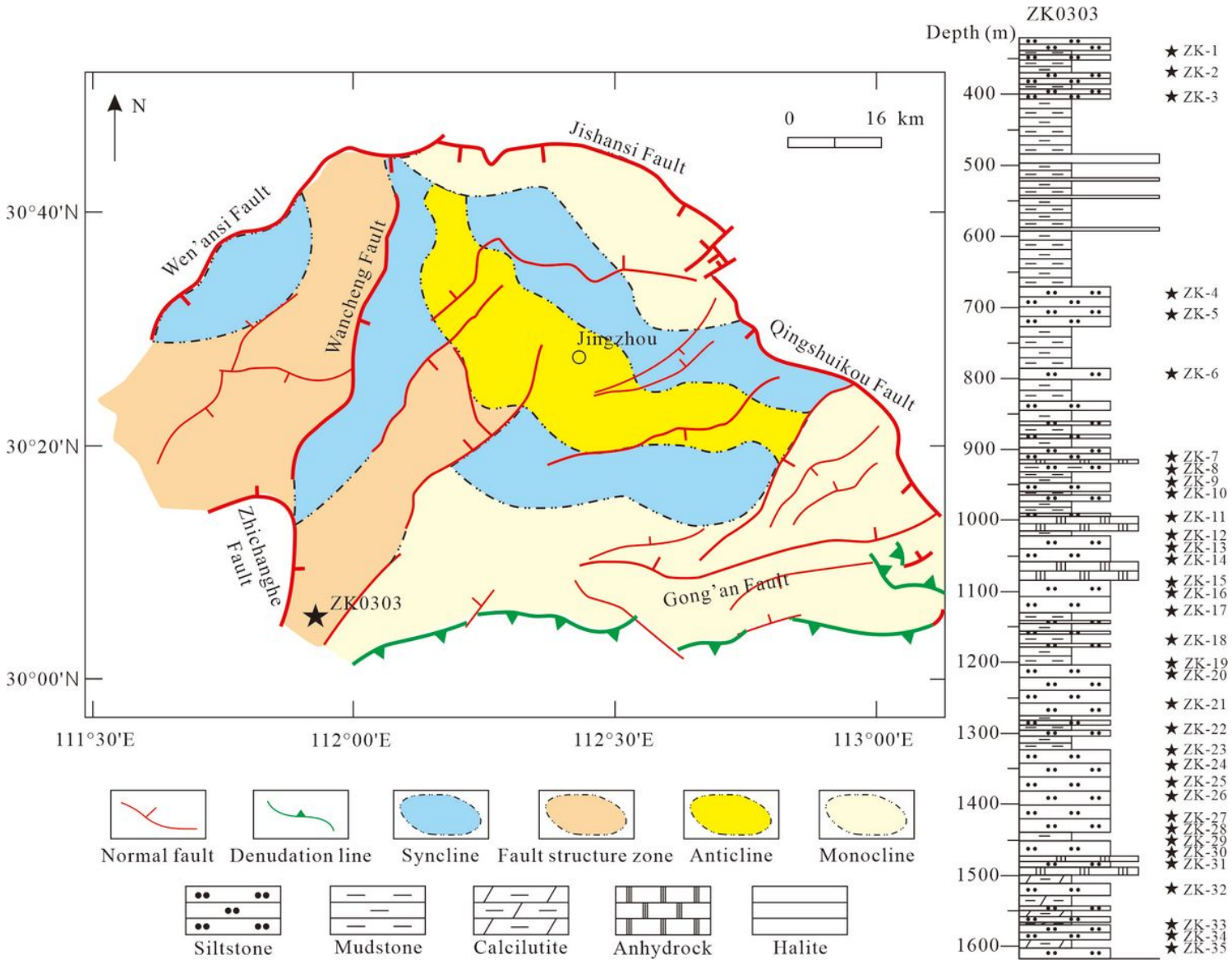

Figure 2

Tectonic map of the Jiangling depression (modified after Teng et al. 2019), and Stratigraphic column of the Shashi Formation in ZK0303.

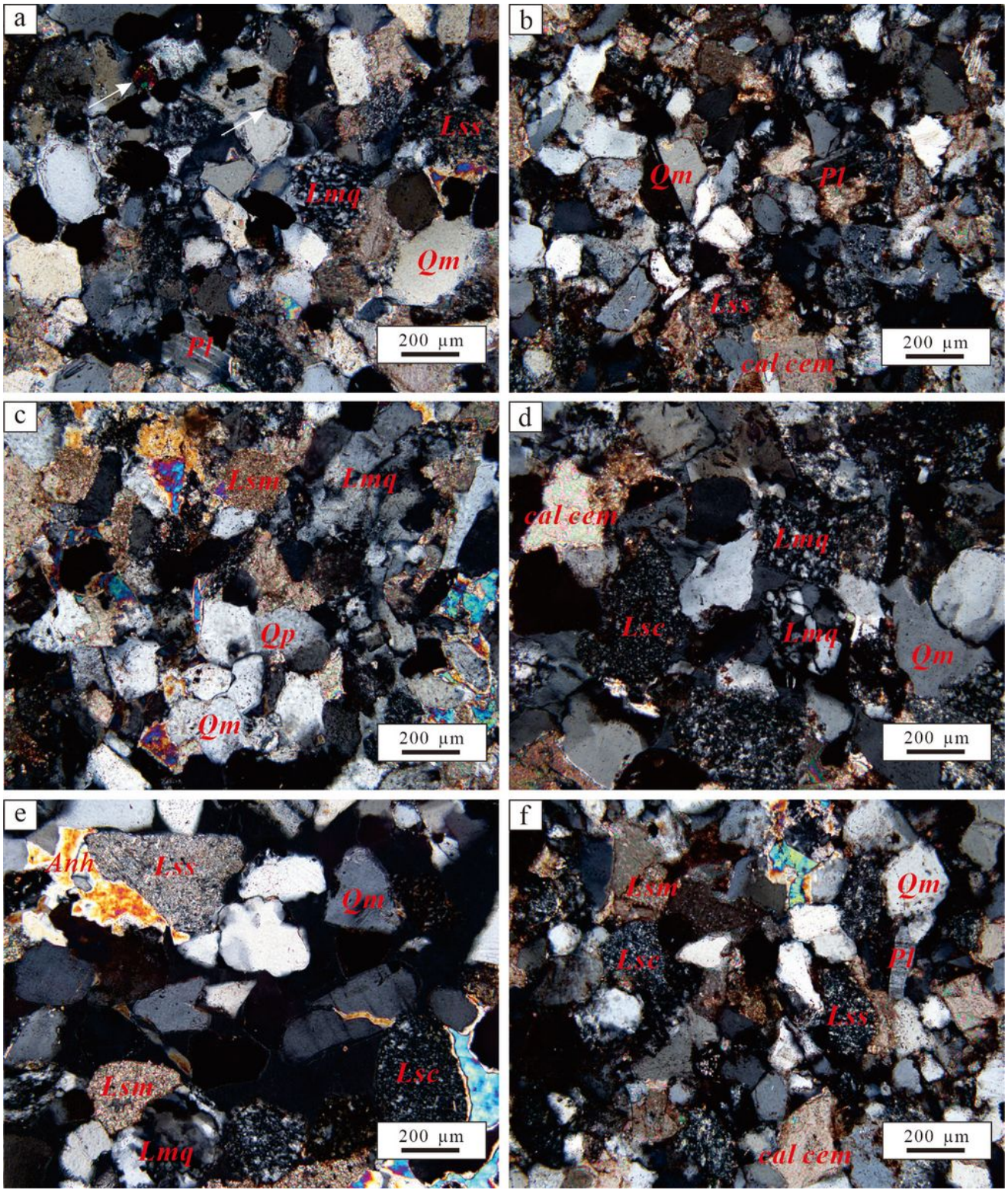

Figure 3

Photographs of siltstone in 320-1600m of Well ZK0303. a: the fragments is mainly monocrystalline quartz, followed by grains of silty mudstone and metamorphic quartz, with a small amount of plagioclase, and heavy minerals (white arrows); b: few quartz with undulose extinction, plagioclase, chert and calcite; c: monocrystalline and polycrystalline quartz, lithic grains are mudstone and metamorphic quartz; d: lithic grains of cherts and metamorphic quartz, cements is mainly calcite; e: sedimentary lithic

grains are mudstone, silty mudstone and chert, metamorphic lithic grain is quartzite; f: monocrystalline quartz, plagioclase, lithic grains are mudstone and chert. Qm: monocrystalline quartz, Qp: polycrystalline quartz, Pl: plagioclase, Lsc: sedimentary chert grain; Lsm: sedimentary mudstone grain, Lss: sedimentary silty mudstone grain, Lmq: metamorphic quartz grain, cal cem: calcite cement, Anh: anhydrite.

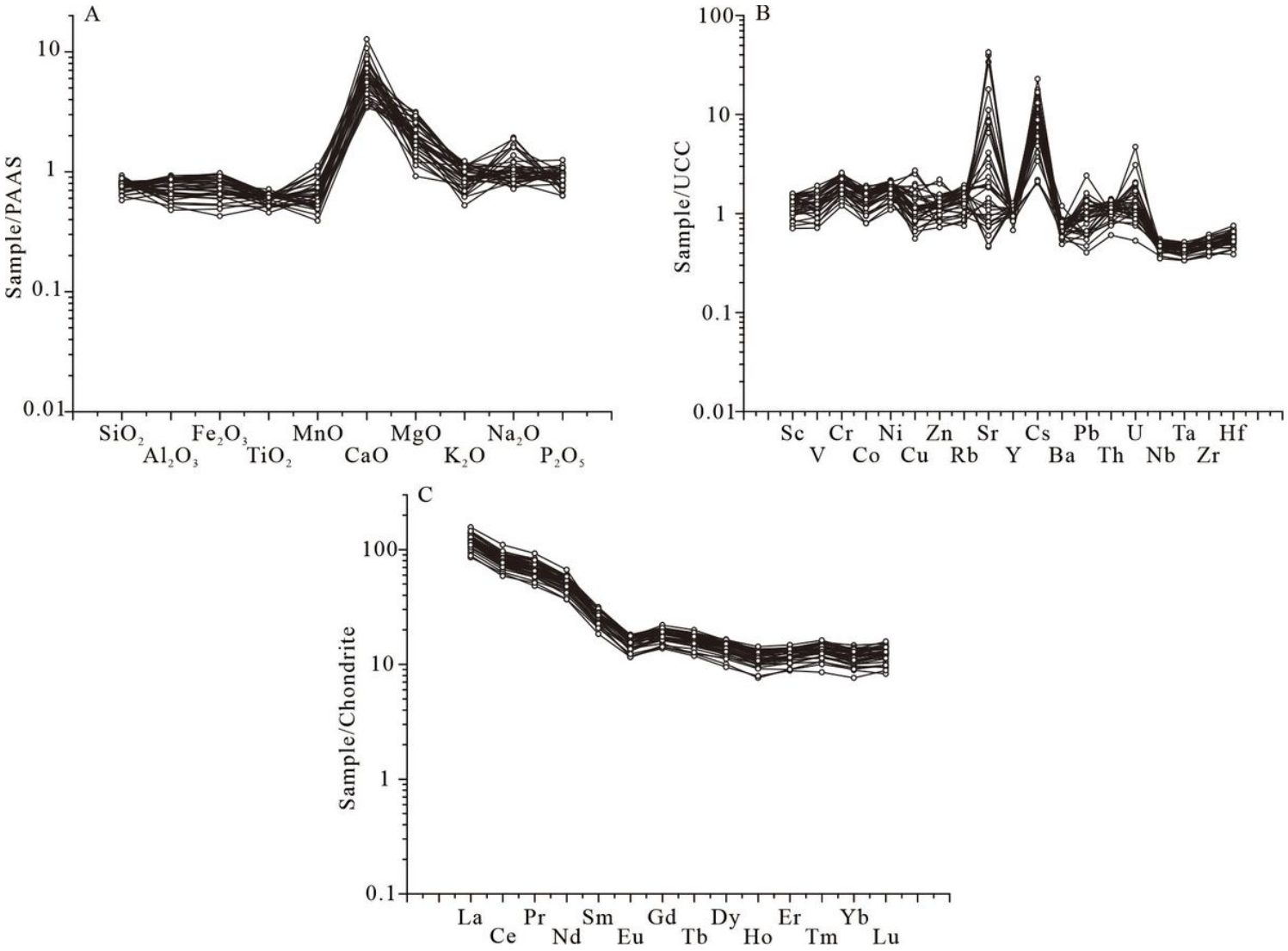

Figure 4

(A) PAAS-normalized major element diagram of samples in Well ZK0303, Data of the PAAS are from McLennan (1989); (B) UCC-normalized trace-element diagram of samples in Well ZK0303, Data of the UC are from Taylor and McLennan (1985); (C) Chondrite-normalized rare element diagram of samples in Well ZK0303, Data of the Chondrite are from Boynton et al. (1984).

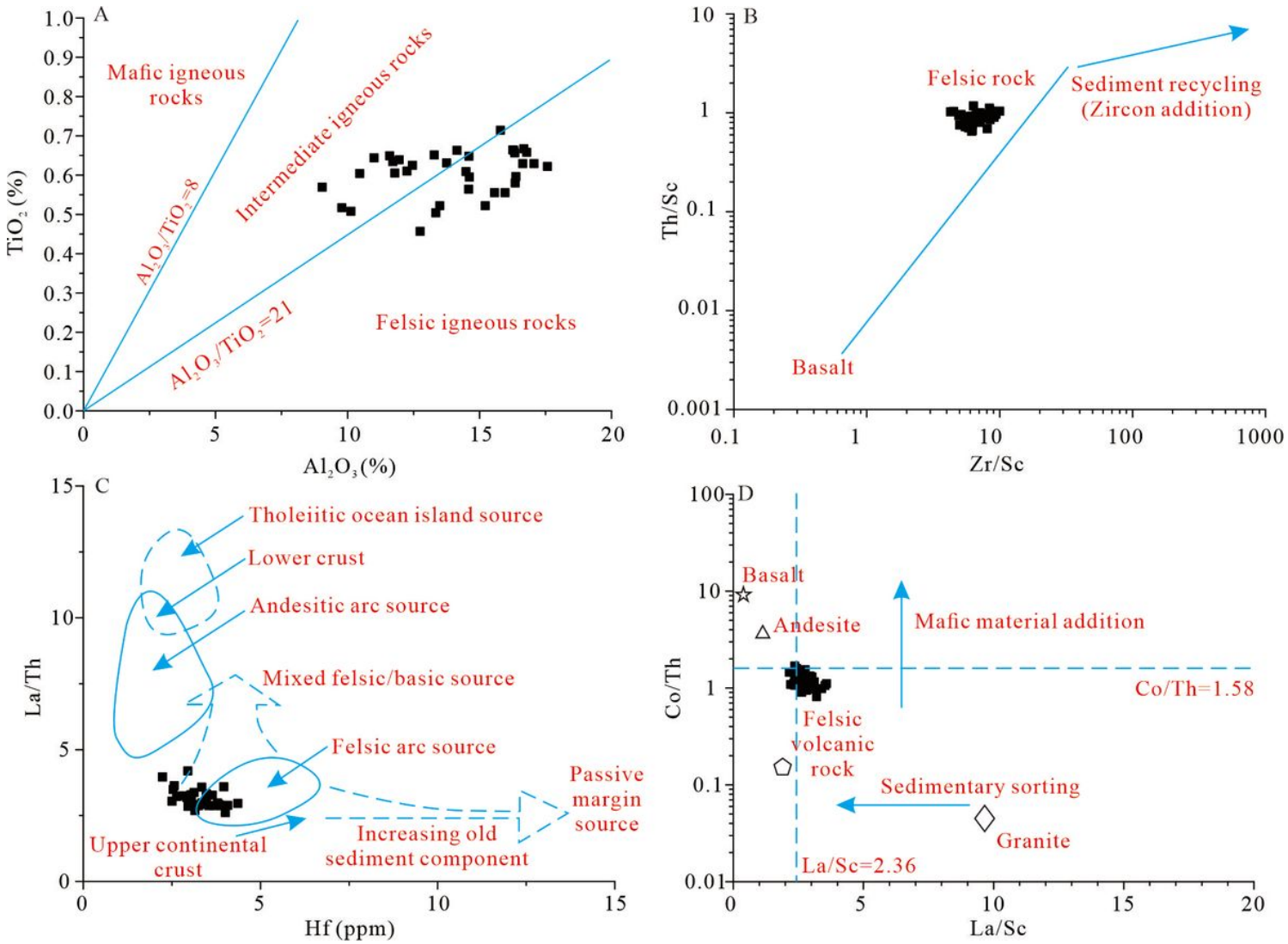

Figure 5

Discrimination diagrams illustrating sedimentary provenance. (A) TiO_2 (%) versus Al_2O_3 (%) bivariate diagram (after Hayashi et al. 1997); (B) Th/Sc versus Zr/Sc bivariate diagram (McLennan et al. 1993); (C) La/Th versus Hf (ppm) bivariate diagram (after Floyd and Leveridge 1987); (D) Co/Th versus Zr/Sc bivariate diagram (after McLennan et al. 1993).

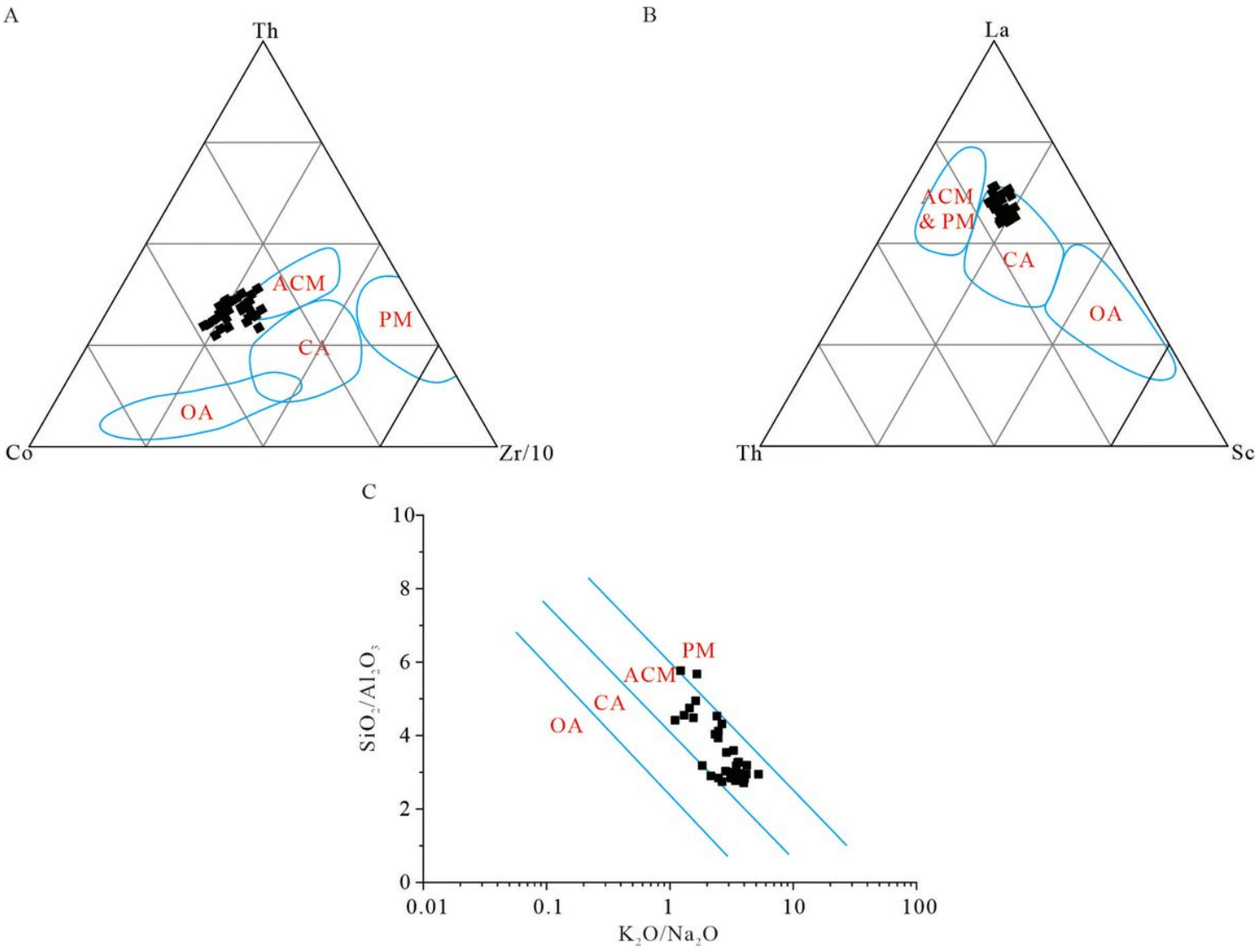

Figure 6

Tectonic discrimination diagrams of samples in ZK0303. (A) Th-Co-Zr/10 ternary diagram (after Bhatia and Crook 1986); (B) La-Th-Sc ternary diagram (after Bhatia and Crook 1986); (C) SiO_2/Al_2O_3 versus K_2O/Na_2O bivariate diagram (after Roser and Korsch 1986). OA: oceanic island arc, CA: continental island arc, ACM: active continental margin, and PM: passive margin.

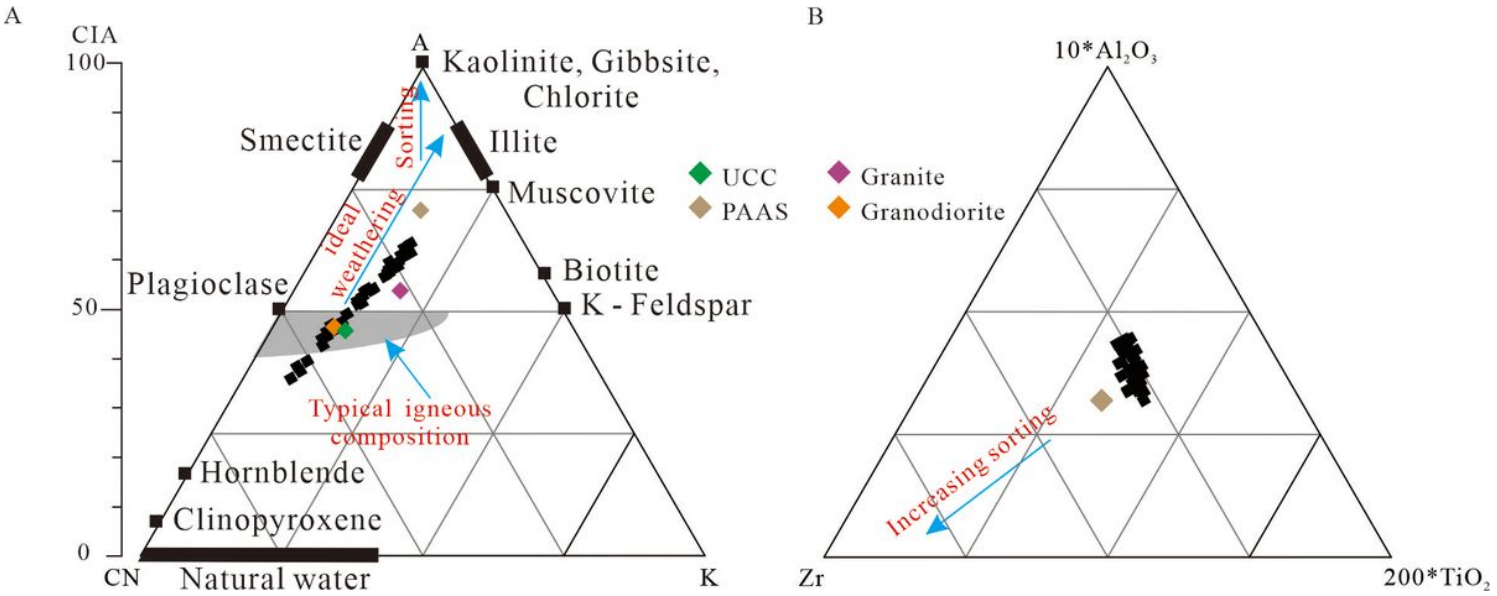

Figure 7

Diagrams showing influence of weathering, sorting processes. (A) Al_2O_3-(CaO + Na_2O)-K_2O (A-CN-K) ternary diagram (after Nesbitt and Young 1984); (B) Al_2O_3-Zr-TiO_2 ternary diagram (after McLennan et al. 1993).

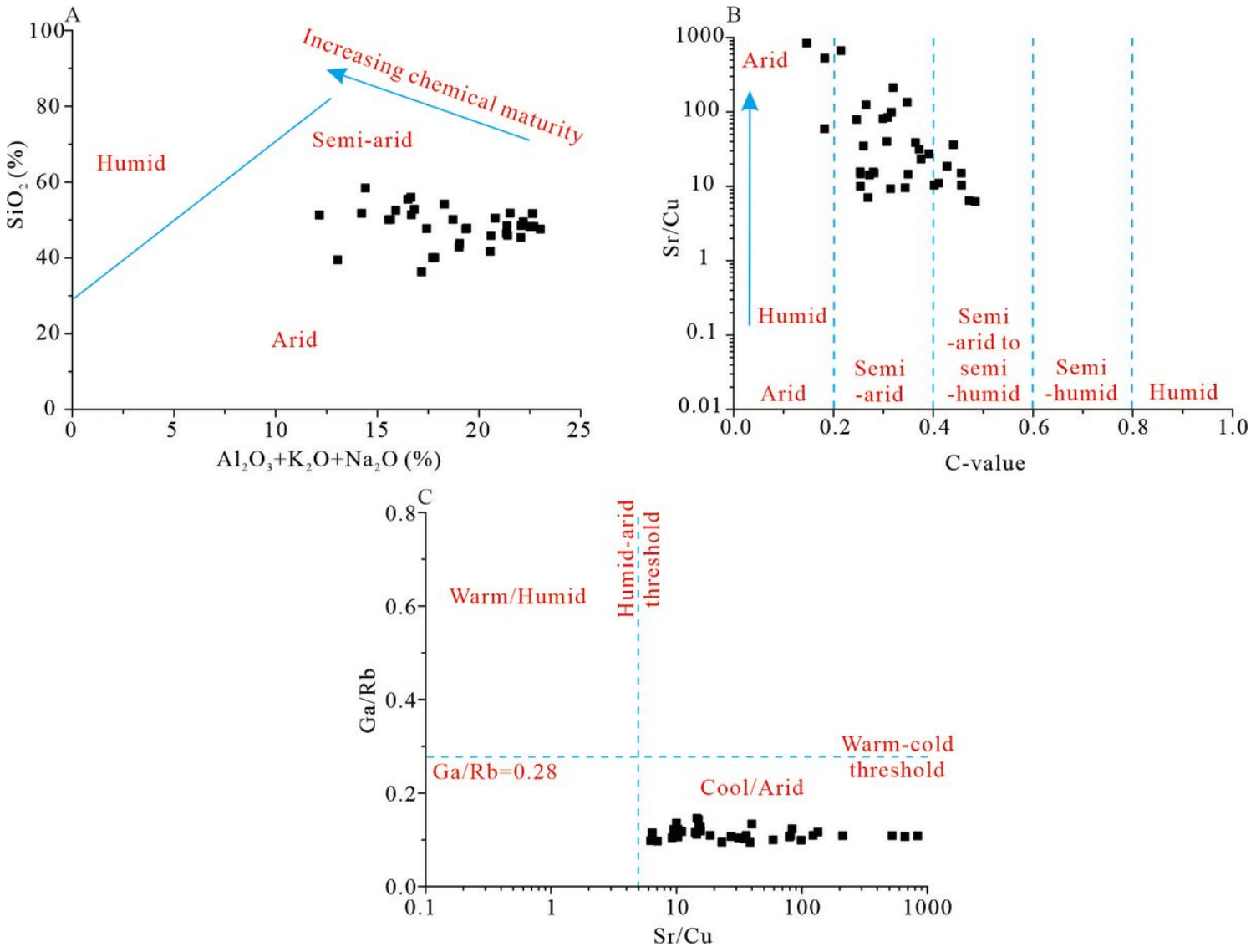

Figure 8

Discrimination diagrams for climatic conditions of samples in ZK0303. (A) SiO_2 (%) versus Al_2O_3+K_2O+Na_2O (%) bivariate diagram (after Suttner and Dutta 1986); (B) Sr/Cu versus C-value bivariate diagram (after Zhao et al. 2007; Cao et al. 2012); (C) Ga/Rb versus Sr/Cu bivariate diagram (after Sarki Yandoka et al. 2015).

Supplementary Files

This is a list of supplementary files associated with this preprint. Click to download.

- SupplementaryTableS1.xlsx